Asian Journal of Chemistry; Vol. 32, No. 3 (2020), 519-527

ASIAN JOURNAL OF CHEMISTRY

https://doi.org/10.14233/ajchem.2020.22406

Co-Doped SnO_2 Supported on Activated Carbon: An Efficient Solar Photocatalyst for the Degradation of Rhodamine B

S.R. KANDE[1], B.H. ZAWARE[1], G.G. MULEY[2] and A.B. GAMBHIRE[3,*]

[1]Research Centre, Department of Chemistry, New Arts, Commerce and Science College, Ahmednagar-414001, India
[2]Department of Physics, Sant Gadge Baba Amravati University, Amravati-444602, India
[3]Department of Chemistry, Shri Anand College, Pathardi-414102, India

*Corresponding author: Fax: +91 2428 223033; Tel. +91 2428 222736; E-mail: abg_chem@ymail.com

Received: 20 August 2019; *Accepted*: 1 October 2019; *Published online*: 31 January 2020; AJC-19752

A series of SnO_2/activated carbon (AC) nanomaterials were prepared by co-doping V(III), Cr(III), Mn(II), Fe(III), Co(III), Ni(II), Cu(II), Zn(II) with nitrogen and sulphur, separately by co-precipitation method, combined with surfactant incorporation method. The as-prepared sample were characterized by X-ray diffraction (XRD), transmission electron microscopy (TEM), X-ray photoelectron spectra (XPS), Brunauer-Teller method (BET), diffuse reflectance spectroscopy (DRS), photoluminescence (PL) and Raman spectroscopy. The results showed that the phase composition, crystallite size, BET surface area and optical absorption of samples varied significantly with the nature dopants. The photocatalytic activities of these co-doped SnO_2/AC catalysts were investigated by degradation rhodamine B in aqueous solution under solar-light illumination. The results showed an appreciable enhancement in the photoactivity of Fe/N/SnO_2/AC as compared to other co-doped SnO_2/AC because of smaller particle size, higher specific surface area, photogenerated carrier's separation and solar light absorption. The degradation rate of rhodamine B dye reached 98 % in 30 min, which is about 10 times higher than that of pure SnO_2.

Keywords: Activated carbon, Co-dopant, Rhodamine B, Solar photocatalysis,

INTRODUCTION

Advanced oxidation process using heterogeneous semiconductor photocatalysts for the wastewater degradation have attracted the researchers in last few decades [1-4]. Strong oxidizing potential, high stability, less toxicity of TiO_2 semiconductor photocatalyst has received great attention. Due to high band gap (3.2 eV) of TiO_2 limits the use of solar light (3-5 %) for the excitation of photons [5,6]. Moreover, high recombination rate of photoexcited e/h pair also hinders the photocatalytic efficiency and commercialization of photocatalyst in bulk quantity. The photocatalytic efficiency of photocatalyst is strongly depends on the separation of these photoexcited e/h pairs [7]. Therefore, to develop an efficient photocatalyst for its commercial application the effective separation of these e/h pairs is necessary. Accordingly, the preparation of robust, low cost, solar light active, exhilarating and efficient photocatalyst is the challenge for researchers. The use of natural solar light rather than artificial UV light for the commercial wastewater treatment could be highly beneficial for the human beings. In order to solve this issue, co-doping of metal and non-metal on SnO_2 semiconductor photocatalyst has been studied. This nanocrystalline photocatalyst is expected to solve the low quantum efficiency problem of various semiconductor photocatalysts due to high e/h pair recombination.

In past few decades, several researchers studied the photocatalytic activity of various photocatalysts such as metal or non-metal doped SnO_2 loaded on carbon based materials such as Cu_2O/SnO_2/graphene [8], CNTs/SnO_2 [9], dye-graphene-SnO_2 composites [10], N-, S-, and C-doped SnO_2 nanoparticles [11], Ge, Si and SnO_2 on TiO_2 ultra-thin films [12], graphite-like carbon supported on SnO_2 [13]. The combination of SnO_2 and supporting carbonaceous material creates heterojunction at their interface. This interface allows the flow of electrons from SnO_2 to carbon with respect to their energy level structure. This heterojunction at their interface decreases the e/h pair recombination. However, a study of photocatalytic degradation of dye using transition metals co-doped SnO_2 also reported in the literature [14].

Till this date, an artificial UV light has been used as an energy source in the photocatalysis research. This is not an economical solution for the wastewater treatment in bulk quantity. To solve this issue, in the present study use of natural solar light for the degradation of rhodamine B dye have been focused.

EXPERIMENTAL

Synthesis of M-nM-co-doped SnO_2/AC photocatalyst: For the synthesis of metal(M)-nonmetal(nM)-co-doped SnO_2/AC nanocrystalline photocatalyst by co-precipitation method, metal nitrates of V(III), Cr(III), Mn(II), Fe(III), Co(III), Ni(II), Cu(II), Zn(II), ammonia and thiourea were used as a dopant precursor. Stannic chloride (99 %, Sigma-Aldrich) was used as a starting material for SnO_2. Respective metal nitrates along with $SnCl_4 \cdot 5H_2O$ were mixed in 1:2 molar ratio. This mixture if dissolved in minimum quantity of deionized water. Cetyltrimethylammonium bromide (CTAB), (20 %, 10 mL) in ethanol is used as a cationic surfactant and added dropwise in the above dissolved solution. The pH of the above solution maintained at 7 by the addition of ammonia solution (30 %) as a source of nitrogen with constant stirring. The formation of precipitate takes place after neutralization. Further, 20 g activated carbon was added with constant stirring and then transferred to ultrasonication for 1 h. The formed slurry was kept to 5 days for ageing. The slurry is further concentrated at 80 ºC to form powder. After overnight drying at 110 ºC this powder is again calcined at 400 ºC for 2 h to prepare nitrogen doped M-co-doped SnO_2/AC.

Meanwhile, in the second set of samples to synthesize sulphur doped M-co-doped SnO_2/AC, a certain amount of thiourea was dissolved in 100 mL deionized water containing 2 ml nitric acid, separately. To this mixture $SnCl_4 \cdot 5H_2O$ and metal nitrates was added drop wise in the same molar ratio. In addition to this 0.01 M NaOH was also added dropwise under vigorous stirring. The remaining procedure is similar as the above mentioned.

Characterization: The phase purity and crystal orientation of products were recorded on Brucker D8 Advanced diffractometer using Cu $K\alpha$ radiation source at 40 kV, 30 mA over 2θ range of 20-80º. Transmission electron microscope and high resolution transmission electron microscope images were obtained using TEM; FEI Tecnai F30, HRTEM; FEG operated at 300 kV. The chemical composition of sample was investigated using X-ray photoelectron spectroscopy (ESCA-3000, VG Microtech, Uckfield, UK). The UV-visible diffuse reflectance spectra (DRS) were measured in the range of 400-4000 cm^{-1} using PE Lambda35 spectrophotometer. A Raman spectrometer (Ventuno, Jasco) was employed to identify the structure of the prepared samples. Photoluminescence (PL) emission spectra of prepared photocatalysts at room temperature were obtained using Scinco FluoroMate FS-2. The samples were excited at 467 nm and the emission was scanned between 340-600 nm. BET surface area measurement of samples was carried out by N_2 adsorption/desorption at 77 K using Micrometrics ASAP 2020 Brunaur-Emmett-Teller surface area analyzer.

Photocatalytic activity: The photocatalytic activity of the prepared photocatalyst was evaluated by the degradation of rhodamine B under natural sunlight irradiation. The dye degradation experiment was carried out in the month of April 2019 from 1.00 p.m. to 2.00 p.m. To overcome the variation of intensity of sunlight the experiments were run in sets simultaneously. The intensity of solar light was recorded using lux meter (LX-101A) and it was found in average 91000 Lux. The intensity was measured at the interval of every 15 min and remains constant throughout the experiment. A prepared photocatalyst (20 mg) was dispersed into 50 mL rhodamine B dye solution in quartz vessel. In order to establish equilibrium between adsorption and desorption the mixture was stirred for 2 h in dark. Further, this mixture was exposed to natural sunlight. During irradiation small quantity of mixture was withdrawn periodically at a given irradiation time interval. The concentration of mixture was analyzed using UV-vis spectrophotometer (UV-1900) after centrifugation at 545 nm. The dye degradation efficiency (%) was estimated using the following equation:

$$\text{Degradation efficiency } (\%) = \frac{(C_o - C_t)}{C_o}$$

where, C_o and C_t are the concentration of rhodamine B dye after time 0 and t, respectively during irradiation. The photocatalytic experiments were repeated four times for each sample.

RESULTS AND DISCUSSION

XRD analysis: The XRD patterns of pure SnO_2, N/SnO_2/AC and S/SnO_2/AC are shown in Fig. 1a. All samples shows the sharp peaks at 2θ = 26.6º and 33.91º, corresponding to (1 1 0) and (1 0 1) crystalline phases of tetragonal SnO_2 (JCPDS card No. 41-1445). The peaks were observed as broad, this attributes the formation of nanocrystalline SnO_2. In the case of M-nM-co-doped SnO_2/AC nanomaterials (Fig. 1b-c), separate phases associated with dopant, co-dopant or any impurity does not found in the XRD pattern. It is observed that with the addition of dopants on SnO_2/AC, the XRD peak shift towards the lower 2θ value and also shows decrease in full-width at half maxima (FWHM) of respective samples (Fig. 1d).

The average particle sizes of the samples were calculated using Debye-Scherrer formula based on the XRD peak broadening analysis at (1 1 0) peak [15] as displayed in Table-1. The particle size of nitrogen and sulphur doped Cr/SnO_2/AC, Mn/SnO_2/AC, Co/SnO_2/AC, Ni/SnO_2/AC, Cu/SnO_2/AC was calculated separately and found to be 20-25 nm. Whereas, V/SnO_2/AC, Fe/SnO_2/AC, Zn/SnO_2/AC samples shows about 10-15 nm. It is also well-known that the least particle size of samples have high surface area. Accordingly, nitrogen and sulphur doped V/SnO_2/AC, Fe/SnO_2/AC and Zn/SnO_2/AC ensure enhanced photocatalytic efficiency.

TEM analysis: To study the effect of co-doping of metal and nonmetal on SnO_2 crystal as well as on their particle size V/N/SnO_2/AC, Fe/N/SnO_2/AC and Fe/S/SnO_2/AC samples were characterized using TEM. The TEM and HRTEM images of (a) V/N/SnO_2/AC, (b) Fe/N/SnO_2/AC, (c) Fe/S/SnO_2/AC samples along with Fourier transfer pattern (FTT) image are displayed in Fig. 2a-f. The particle size of synthesized nanocomposites was found to be about 10-15 nm. Highly mesopores crystalline nanoparticles were observed in the HRTEM images of V/N/SnO_2/AC, Fe/N/SnO_2/AC and Fe/S/SnO_2/AC samples.

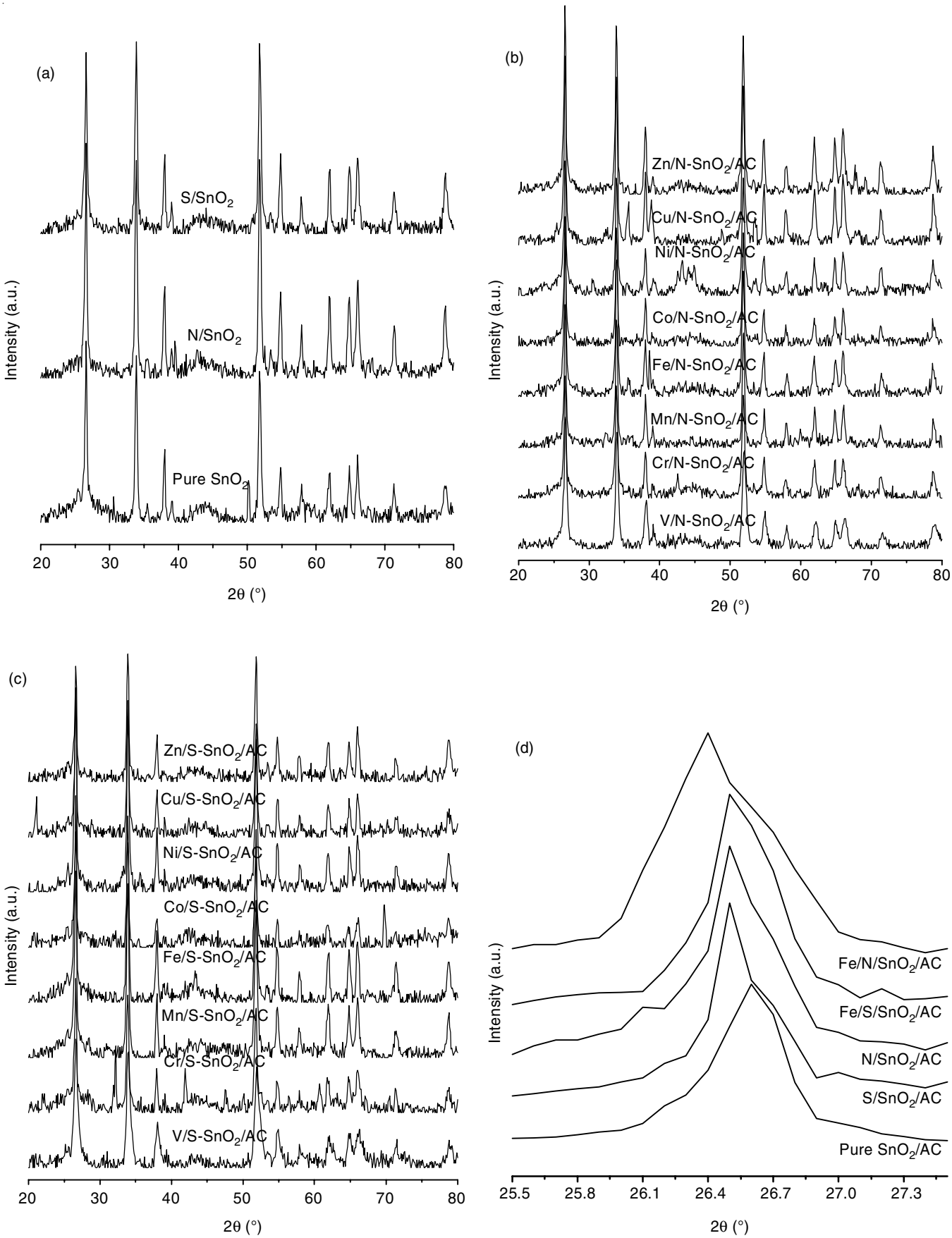

Fig. 1. XRD patterns of (a) pure SnO_2, N-doped SnO_2/AC, S-doped SnO_2/AC, (b) N-doped V-SnO_2/AC, Cr-SnO_2/AC, Mn-SnO_2/AC, Fe-SnO_2/AC, Co-SnO_2/AC, Ni-SnO_2/AC, Cu-SnO_2/AC, Zn-SnO_2/AC, (c) S-doped V-SnO_2/AC, Cr-SnO_2/AC, Mn-SnO_2/AC, Fe-SnO_2/AC, Co-SnO_2/AC, Ni-SnO_2/AC, Cu-SnO_2/AC, and Zn-SnO_2/AC calcined at 400°C for 2 h in air , (d) pure SnO_2/AC, S/SnO_2/AC, N/SnO_2/AC, S/Fe-SnO_2/AC, N/Fe-SnO_2/AC

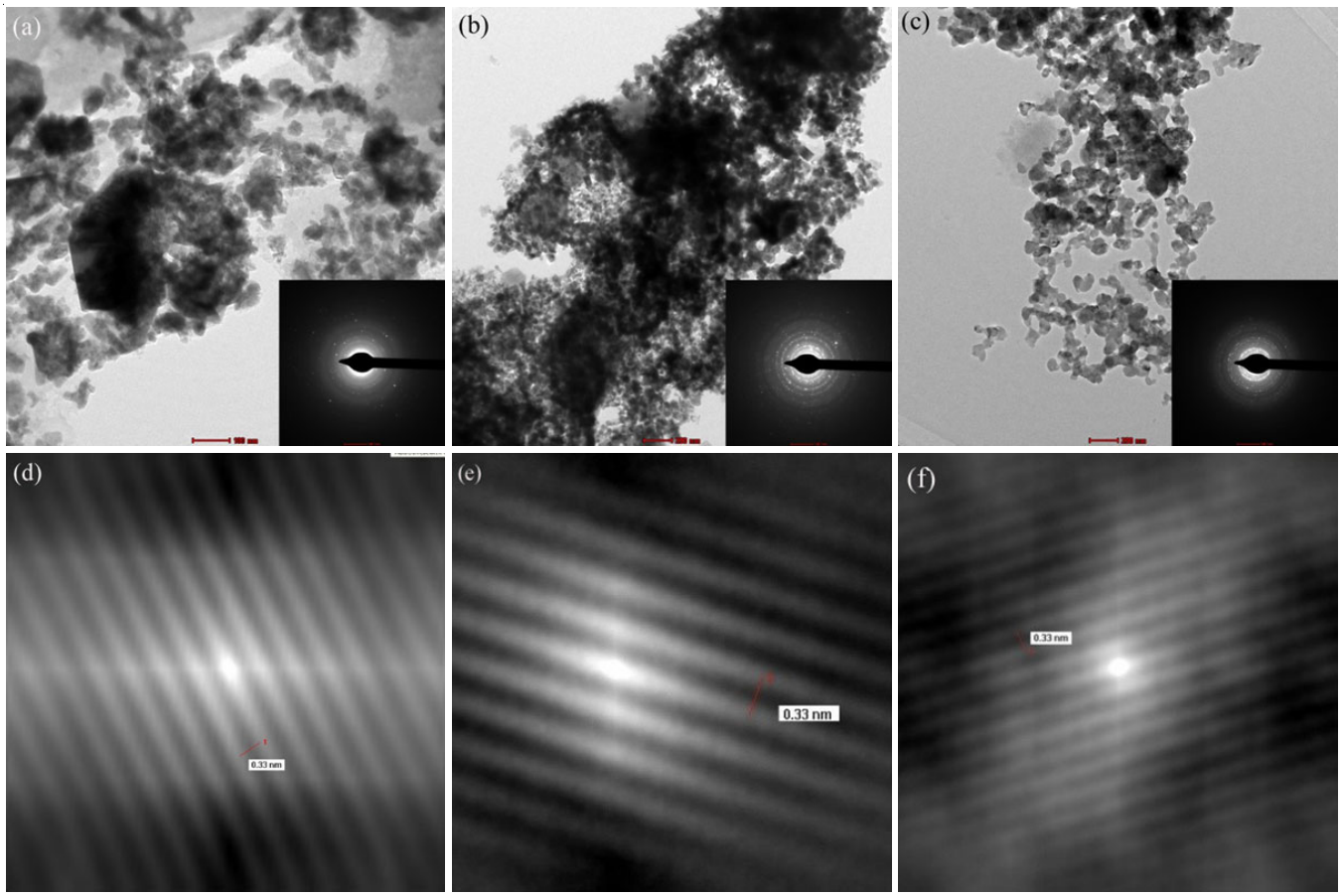

Fig. 2. TEM and HRTEM images of V/N/SnO_2/AC, Fe/N/SnO_2/AC, and Fe/S/SnO_2/AC; TEM images of (a) V/N/SnO_2/AC; (b) Fe/N/SnO_2/AC; (c) Fe/S/SnO_2/AC; HRTEM images of (d) V/N/SnO_2/AC; (e) Fe/N/SnO_2/AC; (f) Fe/S/SnO_2/AC

TABLE-1
BET SURFACE AREA, PARTICLE SIZE OF PREPARED SAMPLES

Samples	BET surface area (m^2 g^{-1})	Particle size (nm)
SnO_2/AC	93.0	20.8
N/SnO_2/AC	110.7	18.2
S/SnO_2/AC	111.5	20.1
V/N/SnO_2/AC	144.1	10.5
Cr/N/SnO_2/AC	127.2	16.9
Mn/N/SnO_2/AC	137.3	17.0
Fe/N/SnO_2/AC	156.7	10.2
Co/N/SnO_2/AC	97.0	18.6
Ni/N/SnO_2/AC	115.9	14.8
Cu/N/SnO_2/AC	122.3	19.0
Zn/N/SnO_2/AC	152.8	12.0
V/S/SnO_2/AC	136.7	11.9
Cr/S/SnO_2/AC	100.6	18.0
Mn/S/SnO_2/AC	91.2	18.1
Fe/S/SnO_2/AC	130.0	13.3
Co/S/SnO_2/AC	111.6	18.2
Ni/S/SnO_2/AC	120.0	14.0
Cu/S/SnO_2/AC	94.0	22.2
Zn/S/SnO_2/AC	141.7	12.7

An interplanar spacing appearing in the micrographs allow the identification of the crystallographic spacing of co-doped SnO_2/AC photocatalysts. These HRTEM images (Fig. 2d-f) shows interplanar spacing of about 0.33 nm corresponding to (1 1 0) crystal plane of SnO_2 [16].

Raman analysis: Raman spectral analysis of Fe/N/SnO_2/AC, Fe/S/SnO_2/AC and Pure SnO_2/AC in the frequency range of 100-3200 cm^{-1} is shown in Fig. 3. The spectra clearly show that both metal and non-metals successfully co-doped on SnO_2 and supported on active carbon. The spectra also show two broad peaks at around 1350 and 1600 cm^{-1}, which are corresponding to active carbon. These are denoted as D and G in the

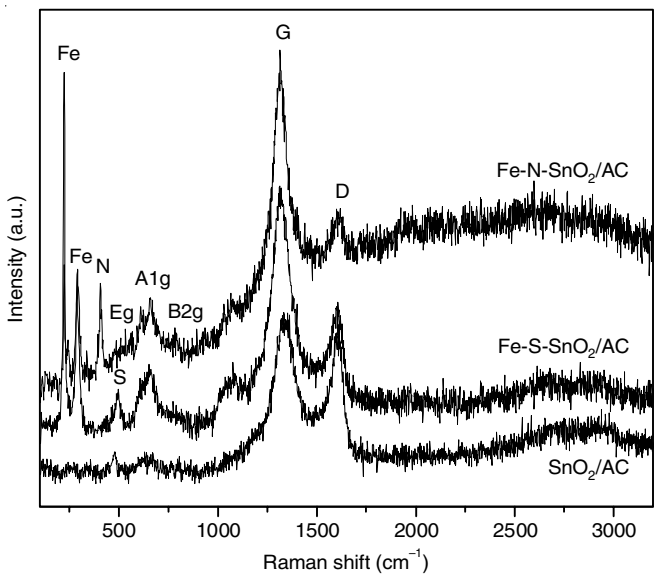

Fig. 3. Raman spectra of M-nM-co-doped SnO_2/AC

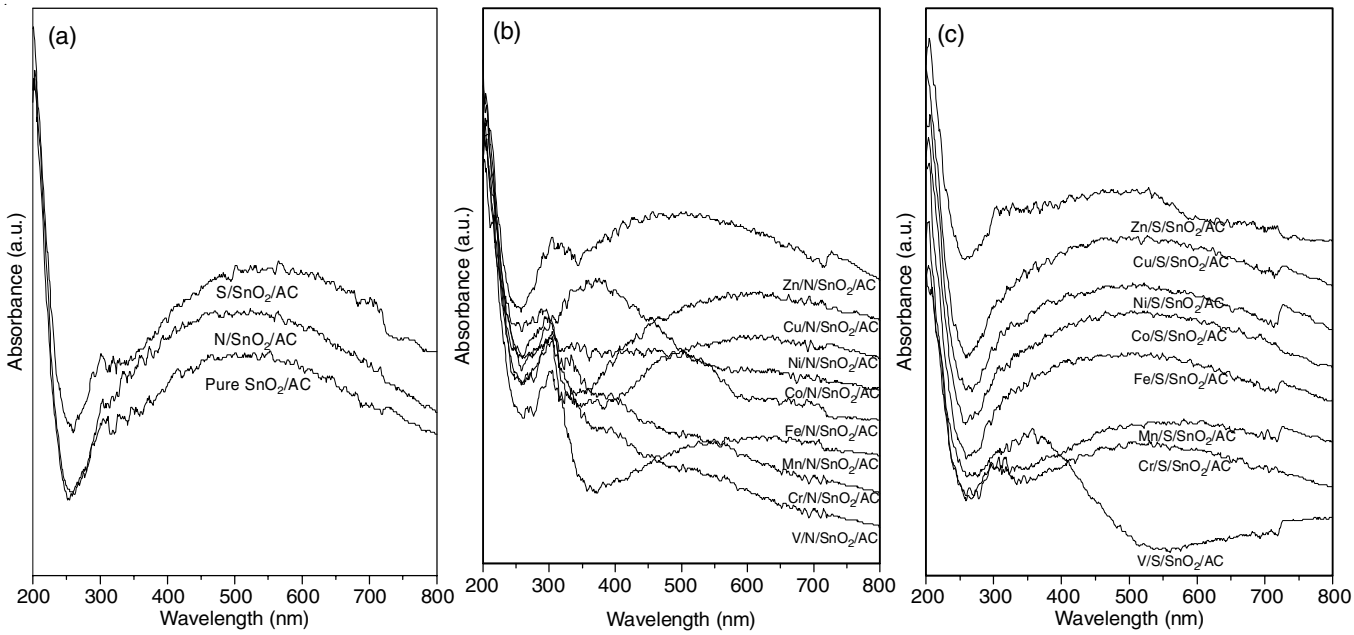

Fig. 4(a-c). UV-Vis-DR spectra of M-nM-co-doped SnO_2/AC

literature. The crystalline quality can be studied from the analysis of peak shapes and selection rule. Based on group theory the normal vibrations modes at the centre of Brillouin zone of tetragonal rutile SnO_2 can be shown as:

$$\Gamma = 1A_{1g} + 1A_{2g} + 1A_{2u} + 1B_{1g} + 1B_{2g} + 2B_{1u} + 1E_g + 3E_u$$

Here four Raman active modes are present, three non-degenerate (A_{1g}, B_{1g} and B_{2g}) and one double degenerate E_g. Two modes (A_{2u} and triply degenerate E_u) are IR active. In addition to this two silent modes (A_{2g} and B_{1u}) are also present. All the samples shows three fundamental peaks which are related to vibration modes at 476 (E_g), 630 (A_{1g}) and 778 (B_{2g}) cm^{-1} of SnO_2 [17]. Nitrogen and sulphur in Fe/N/SnO_2/AC and Fe/S/SnO_2/AC shows peaks at around 399 and 475 cm^{-1}, respectively. The peak at around 222, 294 and 495cm^{-1} corresponds to iron content in the samples [18]. In nano-crystalline SnO_2 system, the surface properties are sensitive not only to the grain size and their distributions but also the oxygen vacancies and local disorder so there may be possibility of the appearance of new modes in the Raman spectra [19]. It is also found that co-doped SnO_2/AC samples shows decrease in the intensities of main peaks this might be due changes in lattice distortion and lattice space symmetry.

UV-visible diffuse reflectance spectral analysis: A UV-vis diffuse reflectance spectrum of the prepared samples is shown in Fig. 4a-c). For all samples, the characteristic absorption peak was detected at 300 nm. After metal and non-metal doping on pure SnO_2/AC the progressive red shift is observed. However, the edges of absorption spectrum of co-doped SnO_2 samples were shifted to near 350 nm which further increases to 500 nm corresponding to 2.25 eV band gap energy. UV-visible DRS spectrum shows that co-doping of metal as well as non-metal on SnO_2/AC increases its absorption towards visible region.

Photoluminescence analysis: The intensity and spectral content of photoluminescence analysis is important tool for probing, chemical composition, charge separation and determination of band gap of semiconducting photocatalysts. The higher photoluminescence intensity means more generation of photogenerated carriers with high rate of electron-hole pair recombination. On the other hand, lower photoluminescence intensity indicate that the rate of electron-hole recombination is low, which is advantageous to the photocatalytic activity [20,21]. Fig. 5 shows the photoluminescence spectrum of selected photocatalysts at excitation wavelength of 210 nm. All the samples show intense emission peaks at 367, 390 and 470 nm. The characteristic near band edge emission of SnO_2 at around 390 nm is matched closely with the reported SnO_2 band gap values [22]. The energy peak appeared at 367 nm corresponds to electron transition, mediated by defect levels in the band gap [23].

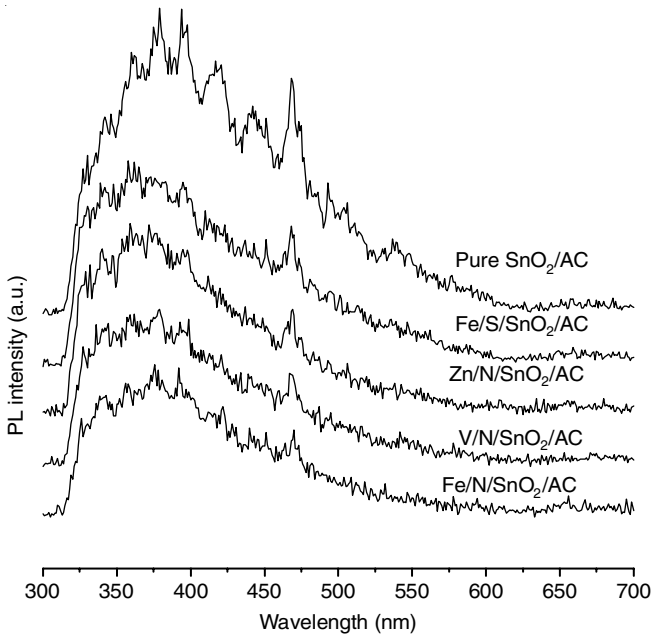

Fig. 5. Photoluminescence (PL) spectra of Fe/N/SnO_2/AC, V/N/SnO_2/AC, Zn/N/SnO_2/AC, Fe/S/SnO_2/AC and pure SnO_2/AC

The emission peak at 470 nm attributes singly charged oxygen vacancies [24]. In addition to this, some small emission peaks appeared in visible region because of formation of luminescence centers in the Sn lattice. It is clearly observed in the graph that Fe/N/SnO_2/AC exhibit weaked emission peak than that of V/N/SnO_2/AC, Fe/S/SnO_2/AC, Zn/N/SnO_2/AC and pure SnO_2/AC. The recombination of photo-induced electron-hole pair in the semiconductor is responsible for photoluminescence of photocatalyst and photoluminescence intensity is directly proportional to the recombination rate of photogenerated e/h pair. This attributes Fe/N/SnO_2/AC has lowest rate of electron-hole pair recombination.

XPS analysis: Further, XPS spectra of V/N/SnO_2/AC, Fe/N/SnO_2/AC, Zn/N/SnO_2/AC and Fe/S/SnO_2/AC compounds were studied to investigate the chemical composition and binding state. Fig. 6a-d reveals the characteristic peaks at 516.8 eV (vanadium), 713.8/715.8eV (iron) and 1022.1/1045.2eV (zinc) [25-29] and confirms the existence of metal dopant in the samples. The Fe_{2p} spectrum of Fe/N/SnO_2/AC and Fe/S/SnO_2/AC samples (Fig. 6b-d) shows an increase in the binding energy. Such increment could be attributed to the formation of Fe-O-Sn bond. This may be due to the transfer of electron from Fe(III) to SnO_2 in the sample [26,27]. The observed peaks at 398.6, 399.1 and 400.1 eV corresponding to N_{1s} spectrum of V/N/SnO_2/AC, Fe/N/SnO_2/AC and Zn/N/SnO_2/AC shows the presence of Sn-N-O bond in the prepared samples [28]. The two prominent peaks at ~ 164.5eV and 168.5 eV (Fig. 6d) ascribed to S_{2p} of Fe/S/SnO_2/AC sample raveled S^{4+} and/or S^{6+} are incorporated into SnO_2 crystal lattice in order to replace Sn^{4+} ions [29]. The Sn_{3d} spectra of all the four samples (Fig. 6i-l) assigned the binding energy values at 485.7, 485.8, 486.2 and 486.4 eV, respectively. As compared to SnO_2 (486.9 eV), lowering in binding energy values signifies the deficiency of oxygen attributes to the incorporation of metal and nonmetal ions into the crystal lattice of SnO_2 lattice [30,31]. The O_{1s} peaks (Fig. 6m-p) centered at 530.8, 531.5, 532.1 and 532.7 eV due to M-Sn-O, O-Sn-O bonding revealed the presence of •OH or adsorbed O_2 molecule [32,33]. As shown in Fig. 6q-t, the C_{1s} spectra

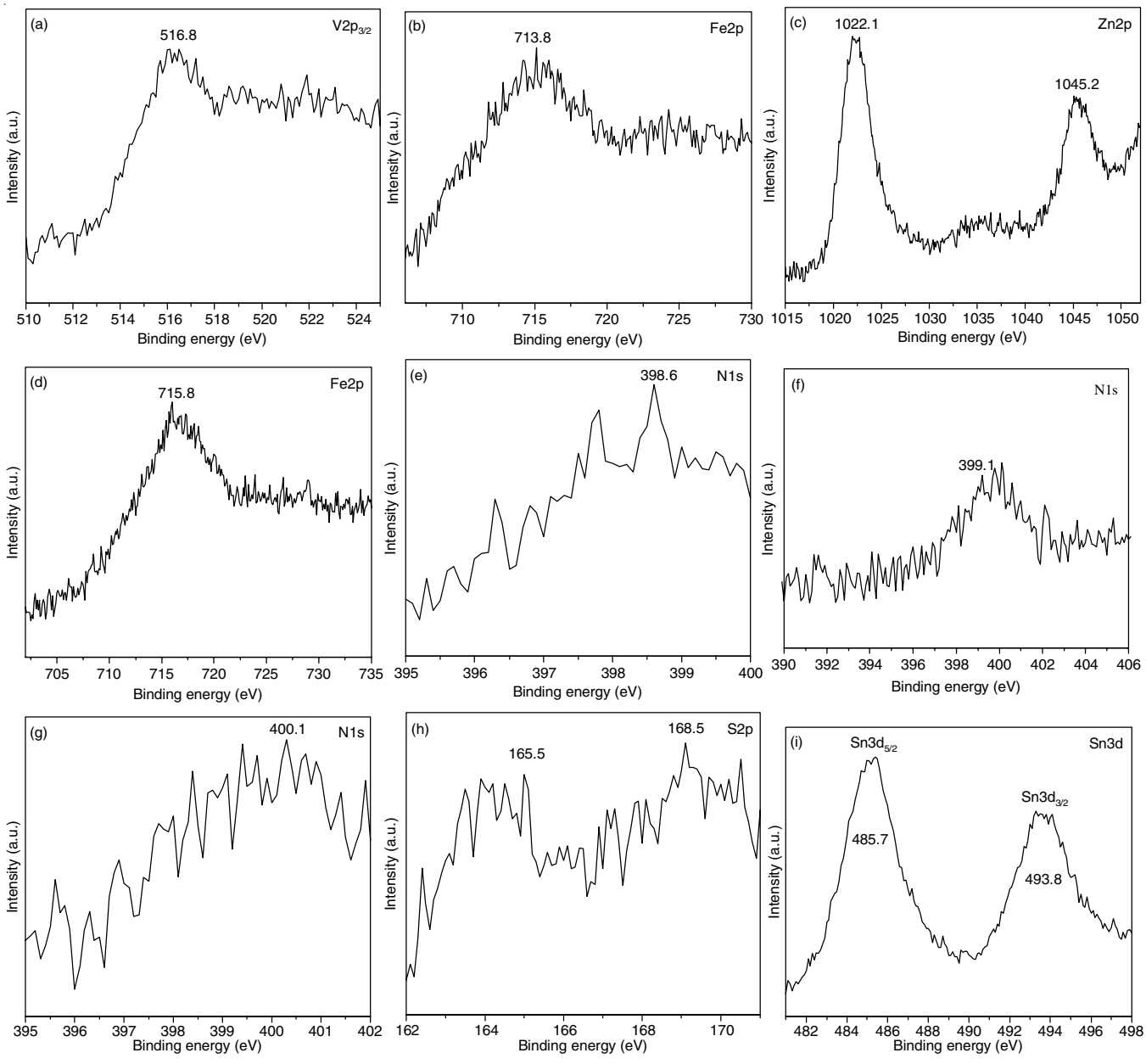

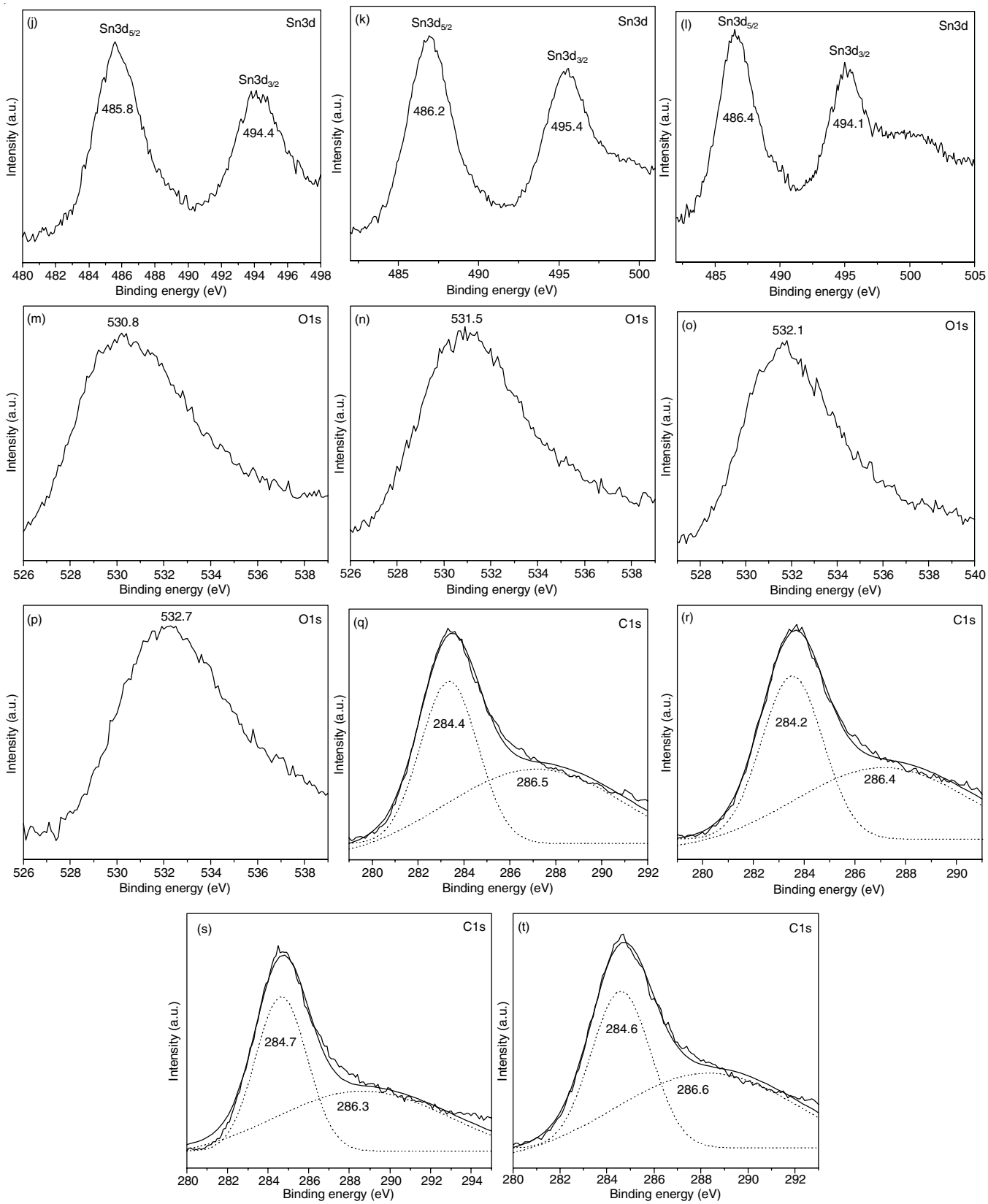

Fig. 6(a-t). High resolution XPS spectra of the $V2p_{3/2}$, Fe2p, Zn_{2p}, O1s, N1s, $Sn3d_{5/2}$, $Sn3d_{3/2}$, C1s region taken on nitrogen-doped V/SnO_2/AC, Fe/SnO_2/AC, Zn/SnO_2/AC and sulphur-doped Fe/SnO_2/AC

showed a asymmetry and broadening towards the higher binding energy side. The spectra can be fitted into two gaussian peaks. In all four samples, lower binding energy peaks positioned at 284.8 eV show the existence of active carbon. The remaining higher energy peaks present at 286.5, 286.1, 286.3 and 286.6 eV correspond to C-O bond formation [34].

Photocatalytic activity: The photocatalytic activities of pure SnO_2, N/SnO_2/AC, S/SnO_2/AC and M-nM-co-doped SnO_2/

AC samples are shown in Fig. 7. Rhodamine B dye degradation was not detected for pure SnO_2 under solar light irradiation. However, the enhancement in rhodamine B dye degradation was observed for N/SnO_2/AC and S/SnO_2/AC samples. Amongst all samples, Fe/N/SnO_2/AC shows the highest photocatalytic activity as only 0.01 % of dye remain undecomposed. While for V/N/SnO_2/AC, Fe/S/SnO_2/AC and Zn/N/SnO_2/AC samples after 30 min irradiation 1-5 % dye remained. In addition to this for nitrogen and sulphur doped SnO_2/AC, Cr/SnO_2/AC, Mn/SnO_2/AC, Co/SnO_2/AC, Ni/SnO_2/AC and Cu/SnO_2/AC 15-25 % dye remain undecomposed. When SnO_2 is irradiated by natural sunlight electron-hole pair get generated. The photogenerated electrons get excited to conduction band and holes remain in valence bond. Large numbers of electron-hole pairs are get recombine with loss of energy. In aqueous medium the photogenerated holes goes to surface and scavenge the adsorbed groups or H_2O molecules to produce highly active radical. This radical is strong oxidizing agent and able to mineralize organic contaminants adsorbed at the surface. The dissolved O_2 molecules in water react with photoexcited electrons in conduction band to generate $O_2^{\bullet-}$ (superoxide ion radical) [35].

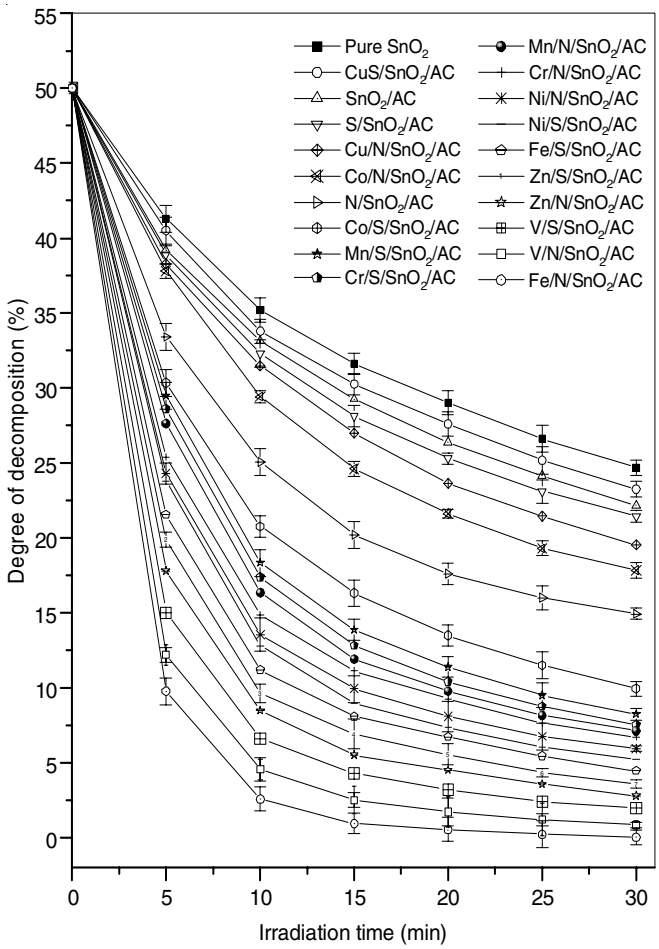

Fig. 7. Rate of decomposition of RhB by using (a) pure SnO_2, (b) N/SnO_2/AC, (c) S/SnO_2/AC, (d) V/N/SnO_2/AC, (e) Cr/N/SnO_2/AC, (f) Mn/N/SnO_2/AC, (g) Fe/N/SnO_2/AC, (h) Co/N/SnO_2/AC, (i) Ni/N/SnO_2/AC, (j) Cu/N/SnO_2/AC, (k) Zn/N/SnO_2/AC, (l) V/S/SnO_2/AC, (m) Cr/S/SnO_2/AC, (n) Mn/S/SnO_2/AC, (o) Fe/S/SnO_2/AC, (p) Co/S/SnO_2/AC, (q) Ni/S/SnO_2/AC, (r) Cu/S/SnO_2/AC, and (s) Zn/S/SnO_2/AC, calcined at 400°C for 2 h in air

$$SnO_2 \xrightarrow{h\nu} SnO_2(e^- + h^+)$$

$$(SnO_2)h^+ + H_2O \longrightarrow SnO_2 + {}^{\bullet}OH + H^+$$

$$(SnO_2)h^+ + {}^-OH \longrightarrow SnO_2 + {}^{\bullet}OH$$

$$(SnO_2)e^- + O_2 \longrightarrow SnO_2 + O_2^{\bullet-}$$

$$O_2^{\bullet} + (SnO_2)e^- + 2H^+ \longrightarrow H_2O_2 + SnO_2$$

$$(SnO_2)e^- + H_2O_2 \longrightarrow {}^-OH + {}^{\bullet}OH + SnO_2$$

After the solar light irradiation on Fe/N/SnO_2/AC, the optical excitation takes place on SnO_2. These photo-excited electrons from conduction band of SnO_2 scavenged to doped Fe and carbon atoms. The creation of oxygen vacancies and e/h pair separation results in the increase in its photocatalytic activity. Furthermore, oxygen vacancies get created into the crystal lattice of SnO_2 and Sn^{4+} ions get replaced by Fe^{3+}. This oxygen vacancy captures the oxygen molecules in aqueous medium. Accordingly, the photogenerated e/h pair gets separate and inhibits their recombination. Here, doped metal atoms accepts the photoexcited electrons, effectively restricts the recombination of e/h pair and promotes the efficiency of photocatalyst. The more adsorption due to high surface area of Fe/N/SnO_2/AC also promotes the RhB dye degradation. The nitrogen and sulphur doped SnO_2/AC, Cr/SnO_2/AC, Mn/SnO_2/AC, Co/SnO_2/AC, Ni/SnO_2/AC and Cu/SnO_2/AC shows more adsorption towards visible region as compared to pure SnO_2. The formation of oxygen vacancies into the crystal lattice of SnO_2 leads to generate the mid gap energy states between conduction and valence band. This trapping of charge carriers into mid gap energy states shows the red shift in absorption.

Moreover, doping of N and S on SnO_2 shows the mixing of N_{2p} and S_{2p} orbital′s with the O_{2p} orbital of SnO_2. This results in the decrease in band gap energy due to the generation of mid gap energy states. The cooperative effect of both N and S on SnO_2 increased the absorption over the whole visible region. This indicates that an absorption could also enhance the efficiency of the photocatalytic reaction since the number of photons participating in the photocatalytic reaction is larger. Moreover, Fe/N/SnO_2/AC sample shows the highest specific surface area *i.e.* 156.7 $m^2 g^{-1}$ indicates high adsorption capacity. Accordingly, Fe/N/SnO_2/AC photocatalyst shows the highest photocatalytic efficiency.

Conclusion

A new co-doped SnO_2/AC nanocrystalline photocatalysts with enhanced photocatalytic activity were successfully synthesized using co-precipitation method combined with surfactant incorporation method. It was observed that as-synthesized samples showed least particle size and high BET surface area. The synthesized nanocrystalline photocatalysts were characterized by advanced techniques like XRD, HRTEM, XPS, UV-DRS, FTIR, photoluminescence and Raman techniques. This is observed that the M-nM-co-doped SnO_2/AC samples showed red shift towards the visible region than pure SnO_2. The Fe/N/SnO_2/AC shows highest photocatalytic activity as compared to other co-doped photocatalysts. The remarkable enhancement in the photocatalytic activity attributes to the synergistic effect of efficient charge separation, high surface area and least particle size.

ACKNOWLEDGEMENTS

This work was financed by Science & Engineering Research Board (SERB), Grant No. SB/EMEQ-029/2014 and DST-FIST, Grant No. SR/FST/College-262, New Delhi, India.

CONFLICT OF INTEREST

The authors declare that there is no conflict of interests regarding the publication of this article.

REFERENCES

1. A. Molinari, E. Sarti, N. Marchetti and L. Pasti, *Appl. Catal. B*, **203**, 9 (2017); https://doi.org/10.1016/j.apcatb.2016.09.031
2. P. Wang, Y. Tang, Z. Dong, Z. Chen and T.T. Lim, *J. Mater. Chem. A Mater. Energy Sustain.*, **1**, 4718 (2013); https://doi.org/10.1039/c3ta01042b
3. H. Shen, X. Zhao, L. Duan, R. Liu, H. Wu, T. Hou, X. Jiang and H. Gao, *Appl. Surf. Sci.*, **391**, 627 (2017); https://doi.org/10.1016/j.apsusc.2016.06.031
4. F. Wang, T. Wang, J. Lang, Y. Su and X. Wang, *J. Mol. Catal. Chem.*, **426**, 52 (2017); https://doi.org/10.1016/j.molcata.2016.11.001
5. J. Lim, D. Monllor-Satoca, J.S. Jang, S. Lee and W. Choi, *Appl. Catal. B*, **152-153**, 233 (2014); https://doi.org/10.1016/j.apcatb.2014.01.026
6. Q. Wali, Z.H. Bakr, N.A. Manshor, A. Fakharuddin and R. Jose, *Sol. Energy*, **132**, 395 (2016); https://doi.org/10.1016/j.solener.2016.03.037
7. R.R. Bhosale, S.R. Pujari, G.G. Muley, S.H. Patil, K.R. Patil, M.F. Shaikh and A.B. Gambhire, *Sol. Energy*, **103**, 473 (2014); https://doi.org/10.1016/j.solener.2014.02.043
8. Z. Wang, Y. Du, F. Zhang, Z. Zheng, X. Zhang, Q. Feng and C. Wang, *Mater. Chem. Phys.*, **140**, 373 (2013); https://doi.org/10.1016/j.matchemphys.2013.03.052
9. N. Wang, J. Xu and L. Guan, *Mater. Res. Bull.*, **46**, 1372 (2011); https://doi.org/10.1016/j.materresbull.2011.05.014
10. S. Zhuang, X. Xu, B. Feng, J. Hu, Y. Pang, G. Zhou, L. Tong and Y. Zhou, *Appl. Mater. Interf.*, **6**, 613 (2014); https://doi.org/10.1021/am4047014
11. A. Nouri and A. Fakhri, *Spectrochim. Acta A Mol. Biomol. Spectrosc.*, **138**, 563 (2015); https://doi.org/10.1016/j.saa.2014.11.075
12. E. Salmani, A. Laghrissi, M. Rouchdi, E. Benchafia, H. Ez-Zahraouy, N. Hassanain, A. Mzerd and A. Benyoussef, *Sol. Energy*, **155**, 18 (2017); https://doi.org/10.1016/j.solener.2017.06.018
13. J. Wei, S. Xue, P. Xie and R. Zou, *Appl. Surf. Sci.*, **376**, 172 (2016); https://doi.org/10.1016/j.apsusc.2016.03.058
14. M.M. Rashad, A.A. Ismail, I. Osama, I.A. Ibrahim and A.-H.T. Kandil, *Clean, Soil, Air Water*, **42**, 657 (2014); https://doi.org/10.1002/clen.201300032
15. A.B. Gambhire, M.K. Lande, S.B. Kalokhe, M.D. Shirsat, K.R. Patil, R.S. Gholap and B.R. Arbad, *Mater. Chem. Phys.*, **112**, 719 (2008); https://doi.org/10.1016/j.matchemphys.2008.06.022
16. L. Chen, J. Xu, Z. Li and J. Xia, *Sol. Energy*, **155**, 593 (2017); https://doi.org/10.1016/j.solener.2017.06.062
17. P.V. Reddy, B.S. Reddy and S.V. Reddy, *Int. J. Chemtech Res.*, **6**, 2568 (2014).
18. S.A. Saleh, A.A. Ibrahim and S.H. Mohamed, *Acta Phys. Pol. A*, **129**, 1220 (2016); https://doi.org/10.12693/APhysPolA.129.1220
19. J. Kaur, J. Shah, R.K. Kotnala and K.C. Verma, *Ceram. Int.*, **38**, 5563 (2012); https://doi.org/10.1016/j.ceramint.2012.03.075
20. I.S. Grover, R.C. Prajapat, S. Singh and B. Pal, *Sol. Energy*, **144**, 612 (2017); https://doi.org/10.1016/j.solener.2017.02.001
21. S. Martha, K.H. Reddy and K.M. Parida, *J. Mater. Chem. A Mater. Energy Sustain.*, **2**, 3621 (2014); https://doi.org/10.1039/c3ta14285j
22. K.V. Anand, R. Mohan, R.M. Kumar, M.K. Chinnu and R. Jayavel, *J. Exp. Nanosci.*, **9**, 261 (2014); https://doi.org/10.1080/17458080.2012.656708
23. V. Salles and S. Bernard, *Nanomater. Nanotechnol.*, **6**, 1 (2016); https://doi.org/10.5772/62161
24. S.S. Shinde, R.A. Bansode, C.H. Bhosale and K.Y. Rajpure, *J. Semicond.*, **32**, 013001 (2011); https://doi.org/10.1088/1674-4926/32/1/013001
25. J. Mazloom, F.E. Ghodsi and H. Golmojdeh, *J. Alloys Compd.*, **639**, 393 (2015); https://doi.org/10.1016/j.jallcom.2015.03.184
26. N.R. Khalid, Z. Hong, E. Ahmed, Y. Zhang, H. Chan and M. Ahmad, *Appl. Surf. Sci.*, **258**, 5827 (2012); https://doi.org/10.1016/j.apsusc.2012.02.110
27. H. Huang, S. Tian, J. Xu, Z. Xie, D. Zeng, D. Chen and G. Shen, *Nanotechnology*, **23**, 105502 (2012); https://doi.org/10.1088/0957-4484/23/10/105502
28. S.S. Pan, G.H. Li, L.B. Wang, Y.D. Shen, Y. Wang, T. Mei and X. Hu, *Appl. Phys. Lett.*, **95**, 222112 (2009); https://doi.org/10.1063/1.3258354
29. L.C. Chen, C.M. Huang, M.C. Hsiao and F.R. Tsai, *Chem. Eng. J.*, **165**, 482 (2010); https://doi.org/10.1016/j.cej.2010.09.044
30. F. Montilla, E. Morallón, A. De Battisti, S. Barison, S. Daolio and J.L. Vázquez, *J. Phys. Chem. B*, **108**, 15976 (2004); https://doi.org/10.1021/jp048674+
31. X. Jia, Y. Liu, X. Wu and Z. Zhang, *Appl. Surf. Sci.*, **311**, 609 (2014); https://doi.org/10.1016/j.apsusc.2014.05.118
32. Y. Qin, J. Xiong, W. Zhang, L. Liu, Y. Cui and H. Gu, *J. Mater. Sci.*, **50**, 5865 (2015); https://doi.org/10.1007/s10853-015-9136-4
33. T. Jia, W. Wang, F. Long, Z. Fu, H. Wang and Q. Zhang, *J. Phys. Chem. C*, **113**, 9071 (2009); https://doi.org/10.1021/jp9021272
34. N.R. Khalid, E. Ahmed, Z. Hong, Y. Zhang and M. Ahmad, *Curr. Appl. Phys.*, **12**, 1485 (2012); https://doi.org/10.1016/j.cap.2012.04.019
35. N. Shanmugam, T. Sathya, G. Viruthagiri, C. Kalyanasundaram, R. Gobi and S. Ragupathy, *Appl. Surf. Sci.*, **360**, 283 (2016); https://doi.org/10.1016/j.apsusc.2015.11.008